PNAS
www.pnas.org

Supplementary Information for

Evolution of the Kondo lattice electronic structure above the transport coherence temperature

S.Y. Jang, J.D. Denlinger, J.W. Allen, V.S. Zapf, M.B. Maple, J.N. Kim, B.G. Jang and J.H. Shim

This PDF file includes:

Figs. S1 to S14
SI references

Contents

(S.1) Broad crossover T regimes

It is important to appreciate that both the Kondo screening and lattice coherence effects are broad crossover phenomena, and to understand where the experimental or theoretical T_K and T^* values lie in relation to their high T *onset* and low T groundstate boundaries of their respective transition regions. Figure S1 illustrates these relative T scales in relation to dilute (single impurity) and Kondo lattice magnetic resistivity profiles from $Ce_{0.01}La_{0.99}CoIn_5$ and $CeCoIn_5$, respectively (1), which we label and define as:

Dilute system:

$T_K{}^{onset}$ = onset of incoherent spin-flip scattering -ln(T) resistivity (mathematically it is infinity)
T'_K = resistivity minimum crossover from phonon-scattering to -ln(T) resistivity
$T_K{}^h$ = effective Kondo temperature including the full sixfold degeneracy of the J=5/2 f-states
T_K= Kondo temperature for groundstate f-level = perturbative to non-perturbative theory crossover
$T_K{}^{gs}$ = onset of fully-screened Kondo singlet ground state

Kondo Lattice:

$T^*{}_{onset}$ = onset of lattice coherence
T^*= resistivity maximum, onset of resistivity downturn
$T^*{}_{gs} = T_{FL}$ = onset of ground state Fermi liquid T^2 resistivity behavior.

www.pnas.org/cgi/doi/10.1073/pnas.2001778117

The single impurity Kondo temperature has a specific mathematical formulation of $T_K = Dexp(1/J_K\rho)$ where D is the band half-width at half-maximum, ρ is the density of states at E_F, and J_K is the anti-ferromagnetic Kondo coupling constant. T_K theoretically corresponds to the crossover between perturbative and non-perturbative Kondo coupling. In general $T_K{}^{gs} < T_K << T_K{}^{onset}$ where T_K is closer to the fully screened ground state than to the high T onset of spin-flip scattering, as illustrated in Fig. S1a. While the mathematical *onset* of -ln(T) behavior is infinity, its experimental manifestation in the resistivity profile is the initial *deviation* from the phonon scattering T^n behavior, which then results in the resistivity minimum at the lower temperature of T_K' ≈200 K. Since T_K is commonly used in the literature as a label for the onset temperature of an experimental property, a key point here is that such usage is contrary to its definition.

The dilute Ce example in Fig. S1a also has an interpretation in terms of the Kondo resonance CEF degeneracy crossover effect described by Cornut and Coqblin (2). At higher temperatures, f-level broadening combined with thermal population of higher CEF levels conspire to transform the system from a small Kondo temperature N=2 degeneracy Kondo resonance to larger effective N=4 and N=6 degeneracy Kondo resonance state(s) with an enhanced T_K. Hence the high T -ln(T) regime above 100 K, which has the same dependence for both dilute and concentrated systems, reflects Kondo scattering from a high T f-state in which all CEF levels are indistinguishable with an effective degeneracy of N=6.

The lattice coherence temperature T^* on the other hand, does not have a microscopically-derived mathematical formulation and is experimentally defined from the resistivity, magnetic susceptibility or specific heat profiles. There are various theoretical investigations of the coherence scale in the literature (3–7). Also, an RKKY-like intersite coupling formulation of lattice coherence, $T^* = cJ_K^2\rho$, has been proposed where c=0.45 is a experimental constant determined from a linear scaling relation constructed between T_K and T^* formulas using an extensive tabulation of experimental T_K and T^* values for many Kondo lattice and heavy fermion systems (8). Similar to the case of T_K' versus $T_K{}^{onset}$, one can argue that the *onset* of lattice coherence is actually higher than the resistivity maximum, i.e. that the resistivity "peak" results from an onset of *deviation* from -ln(T) behavior above the peak maximum with $T^*{}_{gs} << T^* < T^*{}_{onset}$.

The observation that T_K is more closely related to the low T fully screened ground state, while T^* is closer to the higher T coherence onset, helps to understand how it can be that $T_K << T^*$ without violation of the intuitive notion that Kondo screening must *precede* coherence of that scattering process. Here we claim that *partial* screening and *partial* coherence in the broad crossover regimes are important concepts to appreciate in the schematics of Fig. 1b. Fully screened Kondo singlets are *not* a requirement for the onset of lattice coherence, which would require $T_K > T^*$. Instead only the T_K' onset of the long -ln(T) regime of Kondo spin-flip scattering and partial screening is required to precede the onset of lattice coherence, e.g. $T_K' > T^*$.

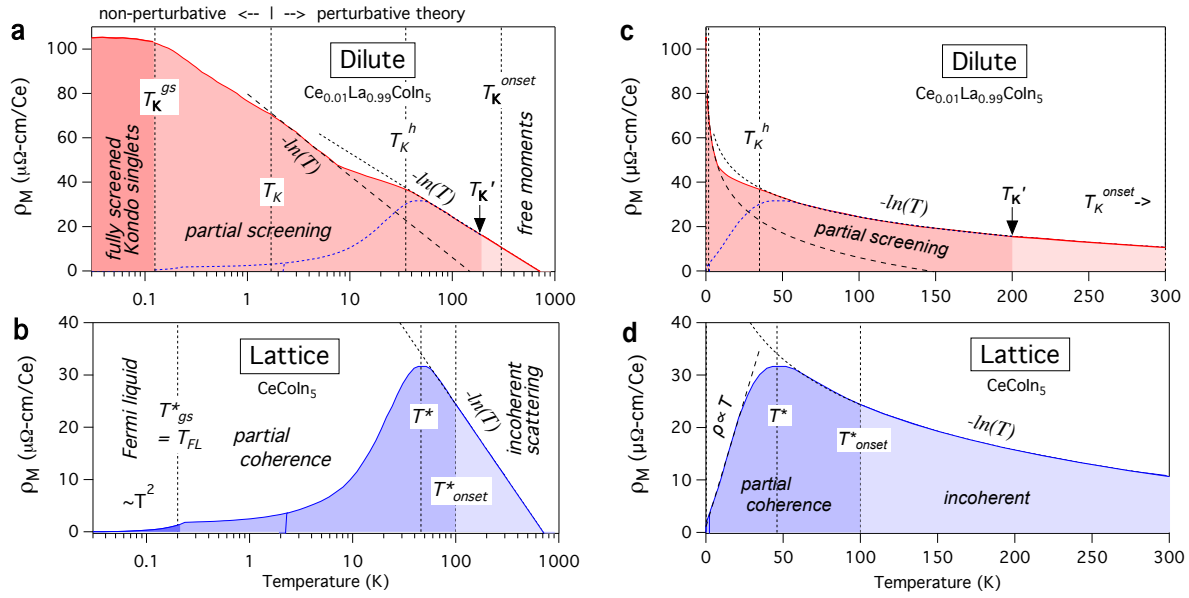

Fig. S1. (a,b) Schematic magnetic resistivity profiles for a dilute impurity (**a**) and a Kondo lattice (**b**) system illustrating the relative relation of the standardly defined temperature scale values of T_K and T^* to low and high T boundaries of the broad crossover regimes of (**a**) Kondo screening and (**b**) lattice coherence. **(c,d)** Linear temperature scale plots of (**a**) and (**b**). Schematics are based on experimental resistivity profiles for $Ce_{0.01}La_{0.99}CoIn_5$ and $CeCoIn_5$ from Nakatsuji *et al.* (1) with additional multiple T_K interpretation applied to the dilute case and a hypothetical extrapolation below the T_c=2.3 K superconducting transition for the lattice. Note also the linearity of the resistivity profile below 20K in (**d**) that is thought to be related to quantum criticality.

(S.2) Z-point 3D Fermi surface

The full theoretical 3D shape of the Z-centered hole-like Fermi surface (FS) is shown in Fig. S2. The experimental confirmation of this complex shape comes from the orthogonal ARPES views from the (001) and (100) cleave surfaces subject to the differing k_z broadening effects. The high symmetry angle map for the (100) surface in Fig. 2d shows the "X" side profile of the FS with k_z-broadened averaging along (010) that enhances the appearance of the thin corner protusions. An ARPES map for the (001) cleave surface at a non-resonant non-high symmetry photon energy of 110 eV with k_z relatively close to the Z-plane, shown in Fig. S2b, exhibits four distinct triangular features about the center that reveal the shape of the thin flat FS protusions. Special attention was paid to avoid surface regions that exhibit In-terminated surface states, shown in Fig. S2c, that obscure the details of this γ_Z FS.

Additionally we show a normal emission photon-dependent k_x-k_z map of the (100) cleave surface in Fig. S2d that complements the angle-dependent k_x-k_z map of Fig. 2e in showing the location of the 122 eV resonance enhancement of the f-weight relative to the concave edge of the Z-centered hole FS. Overplotted DMFT contours provide a guide to this FS which experimentally exhibits parts of the γ contours as well as the diagonal β' feature along the Γ-R direction. Also in Fig. S2e, a 122 eV spectrum measured at 30K and divided by the resolution-convolved Fermi-Dirac distribution (RC-FDD) function to enhance the thermally occupied band structure above E_F, reveals that the two hole-like γ bands cross E_F and form a third f-hotspot involving the higher energy first-excited CEF f-level, in a manner similar to f-c hybridization configurations #2 of Fig. 1c. The close proximity of this higher energy f-hotspot to the γ_Z f-c hybridization configuration #3 causes a large 14 meV dispersion of the f energy level along k_z in the overplotted theory bands, which are in good agreement with experiment, except for an artificial shift to higher energy caused by the RC-FDD division procedure as described in Section S.12.

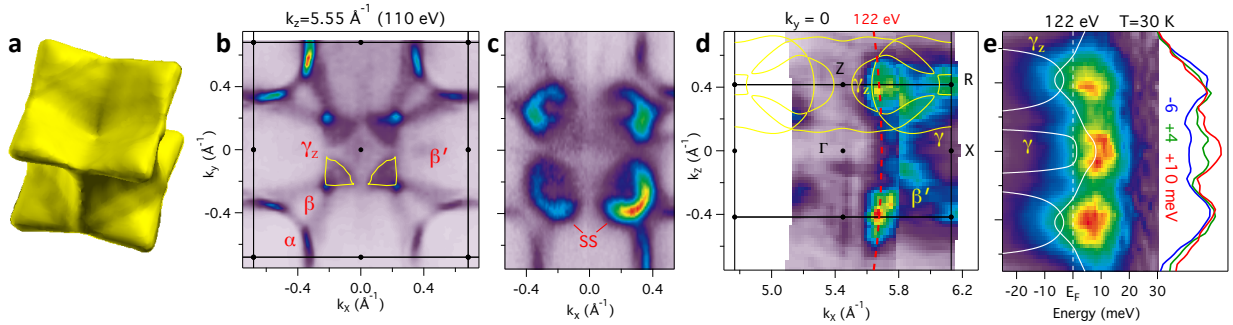

Fig. S2. (a) 3D schematic of the FS topology of the Z-centered hole γ_Z sheet. **(b)** Non-high symmetry 110 eV ARPES (001) E_F map, reproduced from Ref. (9), highlighting the triangular protrusions of the Z-centered hole FS. **(c)** E_F map of a non-optimal region of a (001) cleaved surface that exhibits surface states that obscure the γ_Z FS triangles near normal emission. **(d)** Photon-dependent normal emission ARPES (100) E_F intensity map spanning 97-142 eV, showing the appearance of the 122 eV resonance energy f-hotspots at the edge of the γ_Z FS. **(e)** 122 eV spectra divided by a resolution-convolved Fermi-Dirac profile revealing an additional thermally-excited γ band f-hotspot *above* E_F. Momentum-dependent profiles at select energies below and above E_F also illustrate the development of the central hotspot relative to the outer two γ_Z hotspots.

(S.3) 3D Fermi surface comparison to DFT

Differences in the 3D FS topology derived from this combined ARPES and DMFT (with CEF) study to that of f-itinerant and f-localized DFT calculations is present in Fig. S3. The ARPES/DMFT FS schematics are generated by separately tuning the energy contour of the localized DFT calculation to the desired size consistent with key features of the ARPES measurements and DMFT calculations.

The key notable differences include:

γ-sheet. The hole-like γ FS in the f-localized DFT consists of two separate pieces of tubular sheets along Γ-X in the Γ-plane and a complex-shaped FS centered on the Z-point with a diamond-shaped contour in the Z-plane. In the f-itinerant calculation these hole sheets shrink to become small disconnected FS sheets centered on X and Γ. The ARPES and DMFT-derived FS exhibits an intermediate sized Γ-plane FS where the two FS sheets just touch each other. In addition the a hole-like γ_Z FS similar in shape to the f-localized DFT prediction exists in the ARPES and DMFT, but with f-electron participation. In contrast this sheet is artificially absent in the f-itinerant DFT due to its incorrect unrenormalized f-bandwidth disruption of the near-E_F electronic structure.

β-sheet. The main M-centered electron-like β-sheet is similarly shaped between all three calculations, but with a smaller size for the f-localized calculation. In addition a significantly sized FS sheet along R-Z (labeled β') exists in the f-itinerant calculation as compare to a tiny β' that exists diagonally between R and Γ. The ARPES and DMFT-derived FS also exhibit the f-localized-like diagonal β-sheet but enlarge to become a "finger" connecting to the R-point.

α-sheet. Like the β FS, the main quasi-2D M-centered electron-like α-sheet is similarly shaped between all three calculations, but with a smaller size for the f-localized calculation. In addition a nearly fully-connected along R-Z (labeled α') exists in the f-itinerant calculation but is absent in both the f-localized DFT and the ARPES and DMFT-derived FS.

Another recent T-dependent DFT+DMFT calculation of $CeCoIn_5$ by Nomoto *et al.* (10), a multiband periodic Anderson model constructed from the first-principles GGA band structure, also exhibits a similar absence of an α' FS and finger-like β' FS diagonal along R-Γ, deviating from the f-itinerant DFT shallow electron FS sheets along R-Z. However, still absent from the Nomoto *et al.* DMFT calculation is the γ_Z FS sheet predicted by the DMFT calculation here and experimentally verified by ARPES in Fig. 2e and Fig. S3b.

While the panels in Fig. S3 are visually suggestive of the DMFT FS being *"halfway from the localized to itinerant f band"* and in an *"incompletely itinerant state"* (10), that would be an incorrect conclusion. We reiterate that the main origin of the differences arise from the artificial unrenormalized f-bandwidth errors in the f-itinerant DFT calculation.

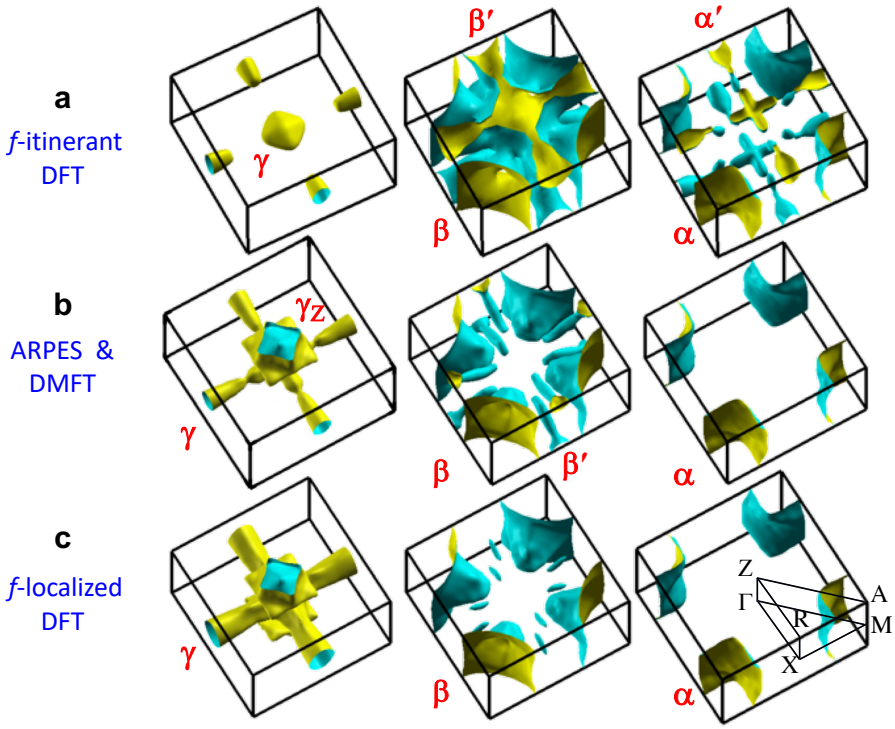

Fig. S3. Comparison of the separate (γ, β, α) three-dimensional FS sheets predicted by (**a**) f-itinerant DFT calculations, (**b**) ARPES and DMFT of this work, and (**c**) f-localized DFT.

(S.4) k-integrated DMFT 4f spectral weight

To complement the narrow 100 meV energy window plot in Fig. 4e of the theoretical k-integrated $4f$ DOS spectral function encompassing only the main Kondo resonance (KR) and CEF sideband peaks, wider energy range DMFT spectra are presented in Fig. S4. Spin-orbit (SO) side bands of the KR are visible at ∼-0.3 eV and +0.4 eV. DMFT f DOS spectra were calculated for 25 temperatures of 10-(+5)-50-(+10)-100-(+20)-200, 250, 300, 400, 500, 750 and 1000 K. The full 12 eV range spectra in the inset for the lowest and highest temperatures additionally show the $4f^0$ electron removal spectral weight extending down to -2 eV and large $4f^2$ electron addition peaks above +2 eV with an integrated area corresponding to ≈12 f electrons.

A striking result of this full energy range plot is the persistence of significant f-weight in the near E_F KR region (including CEF and SO sideband peaks) even at T=1000 K. Analysis of the T-dependent areas of the separate f^0, f^1 and f^2 energy regions indicate that there is less than 10% transfer of spectral weight out of the f^1 KR region from low to high T (primarily to the f^2 region as shown in Fig. S6a). This persistence of high T f-c correlations reflected by the f-DOS in the KR region is consistent with previous single impurity NCA theory calculations (11). Hence the T-dependence of the KR peak(s) is primarily that of decoherence broadening redistribution of spectral weight to tails of the main KR, CEF and SO peaks with a weaker secondary effect of net spectral weight transfer from the KR region to the higher energy lower and upper Hubbard bands. The treatment of the subtraction of this incoherent f-DOS background is important for the comparison to experiment as discussed next.

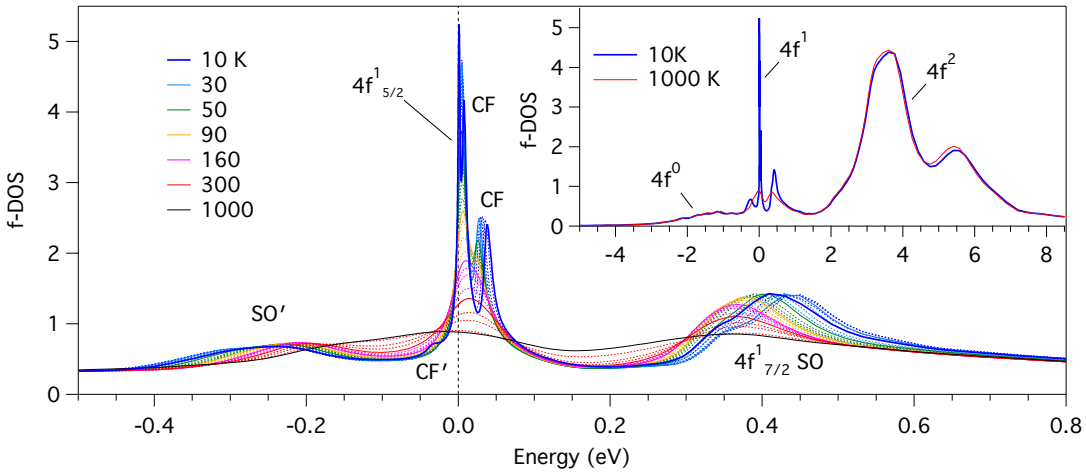

Fig. S4. T-dependent DMFT k-integrated f DOS plotted over wider ∼1 eV and 12 eV (inset) energy ranges, with peak identification labeling of (i) f-removal $4f^0$, (ii) f-addition $4f^2$, (iii) the Kondo resonance (KR) $4f^1_{5/2}$, (iv) spin-orbit (SO) and crystalline electric field (CEF) splittings of the KR, and (v) their sideband excitation peaks (SO′, CF′).

(S.5) T-dependent methods

Temperature dependent measurement procedures employed in this study typically progressed from sample alignment and optimization at 20-40 K, followed by brief cooling to the lowest T, followed by full range warming to the highest T, as shown in Fig. S5a for the (100) surface data of Fig. 4d (cut #3). In addition, thermal cycling measurements including cooling back to the lowest T were also performed to assess surface degradation effects. Figures S5b and S5c show such a thermal cycling measurement between 7K and 64K for the (001) surface hotspot at the similar k-location as the data set Fig. 4c. Typically the f-weight did not fully recover to the original low T amplitude on the final cooldown.

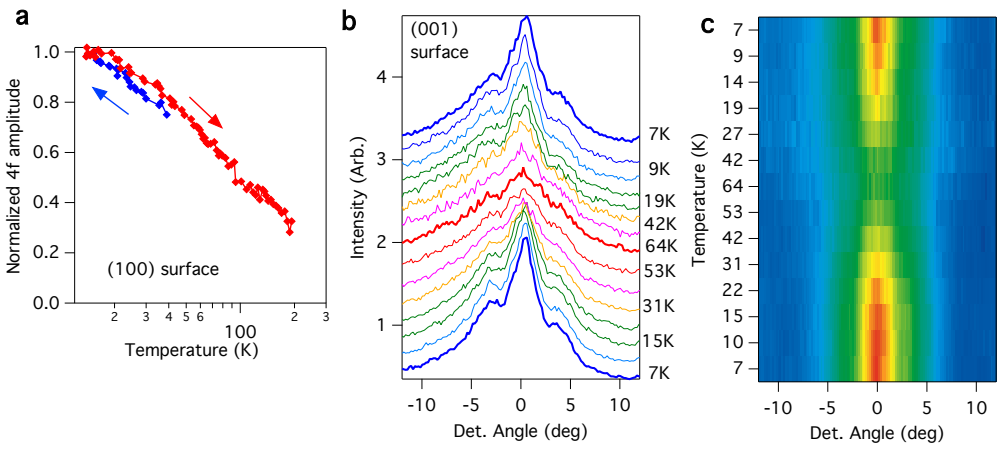

Fig. S5. (a) T-dependent ARPES 4f-amplitude for the (100) surface (cut #3, Fig. 4d data) illustrating the method of initially cooling from 35K to low T before warming to 200K. **(b,c)** T-dependent ARPES 4f-amplitude momentum distribution curves (MDC) and intensity image plot for the (001) surface (cut #2) illustrating a thermal cycling repeatability test.

(S.6) T-dependence Background Subtraction

There are a number of ways to extract the T-dependent f density of states (DOS) from both the ARPES experimental data as well as the DMFT calculations, in terms of peak or E_F amplitude versus peak area, energy versus momentum spectral profile, k-integration window and choice of background subtraction.

DMFT. We wish to not include the high T *incoherent* f-weight. Since significant spectral profile *changes* are still observed up to 750 K, and only minor changes to 1000 K, we choose the 750 K profile for the DMFT background subtraction. Thus inherently the theoretical *coherent* f-DOS T profile will extend to high T before becoming zero at 750 K.

The T-dependent DMFT profile based on the E_F amplitude, with 750K background subtraction and normalization to unity at low T, is very similar to the profile extracted by treating the theory result as a photoemission experiment as shown in in Fig. 4f, i.e. multiplication by the T-dependent Fermi-Dirac distribution (FDD) function, convolution of a Gaussian instrumental resolution broadening, and selection of the f-peak (rather than E_F) amplitude, mainly affects the lowest T saturation part of the profile, as shown in Fig. S6a. We also note that while theoretical f DOS spectra inherently exclude non-f spectral weight, the experimental ARPES backgrounds to be subtracted (discussed next) do include non-f spectral weight.

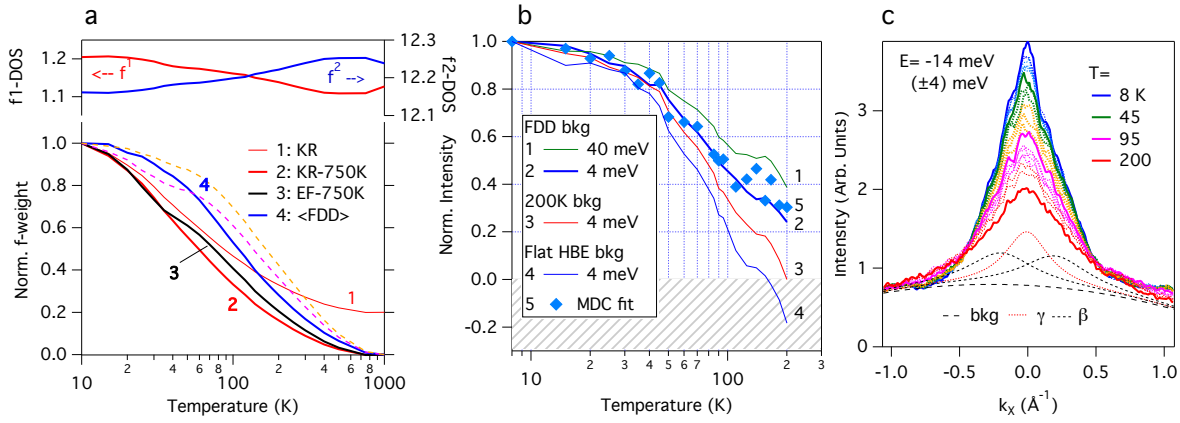

Fig. S6. **(a)** T-dependent DMFT k-integrated 4f-weight. (upper) Spectral weight transfer between f^1 and f^2 regions. (lower) Normalized T-profiles of the main KR peak amplitude (1) without and (2) with 750K background subtraction, (3) the E_F amplitude, and (4) the occupied f-peak amplitude after ARPES-like multiplication by the T-dependent Fermi-Dirac distribution cutoff and instrument energy resolution convolution. **(b)** T-dependent ARPES 4f-weight for the (001) surface ARPES for different methods of background subtraction and different energy integration window widths (see text). **(c)** T-dependent ARPES 4f-amplitude momentum distribution curves (MDC) for a constant binding energy at the hotspot with example 3-component peak fit for the highest T (see text).

ARPES. Figure S6b compares the experimental T-dependent profiles for the (001) surface hotspot shown in Fig. 4b using different analysis backgrounds and energy window integrations. First we use T-dependent FDD energy profiles (convolved with a Gaussian instrumental resolution broadening) for the background of each experimental spectrum, as illustrated for 8 K and 200 K in Fig. 4b. The full occupied f-peak *area* (40 meV integration window up to E_F), shown in profile #1 in Fig. S6b, decreases to only 0.4 at 200 K relative to the low T area normalized to 1. If instead, the f peak *amplitude* (narrow 4 meV energy integration window centered on the peak maximum) is analyzed, the normalized T profile (#2) decreases to almost 0.2 at 200 K. The weaker high T reduction of the peak *area* profile compared to the peak *amplitude* is due to spectral weight transfer to higher binding energy as the peak broadens. Similarly, energy integration of the f-weight *area* including thermal excitation above E_F and spectral transfer into higher CEF f states, further weakens the high T reduction of f weight profile. To avoid the issue of T-dependent spectral weight transfers, we choose to analyze and compare the f-peak *amplitude* as a monitor of the *coherent* f weight changes.

A Shirley integral background, primarily used for core-level background subtraction in photoemission, was also explored for background subtraction but was deemed inappropriate by comparison to the high T DMFT profile. This method increases the total relative f-weight at each T.

Next in profile #3 in Fig. S6b, we explore the concept of using the highest T energy spectrum as a background for subtraction based on the argument that no f-enhancement is visually apparent in the 200 K f spectral image in Fig. 4a. This inherently forces the T profile to go to zero at 200 K. A similar analysis was used in the recent RXS f-weight T dependence, compared in Fig. S7, where an RXS baseline scan above the highest T of 200 K was not available.

Next we compare to a much simpler background subtraction of a constant value based on the high binding energy region around 0.1 eV binding energy, where the experimental spectra have been normalized to unity in Fig. 4b and 4d. Due to the FDD thermal broadening decrease towards E_F, the background level becomes larger than the peak amplitude at high T and the f weight goes to zero at a lower T (∼150 K) and then becomes unphysically negative (profile #4). This method can be viewed as an extremum lower bound to the coherent f-weight T-dependence, which still contains non-zero f-weight extending to $>3T^*$.

Finally, we make comparison to an alternate momentum distribution (MDC) analysis of the (001) surface γ-band hotspot in Fig. S6c using a similar narrow energy integration window of the peak *amplitude*. In this case there is additional uncertainty in the choice of the f-background due to the presence of the outer β-band crossings which produces a triangular-shaped MDC profile. An attempt to separate out the two side β contributions using a three component Lorentzian peak fit to the MDC profiles, produces a γ-band T-dependence (profile #5) that is very consistent with the energy spectrum FDD background subtracted amplitude profile (#2).

Thus, with consideration of the above analysis method sensitivities, we chose to compare in Fig. 4e of the main text the *amplitude* of the experimental f-peak with narrow energy integration window width to the DMFT Fermi-edge spectral weight *amplitude*, with background subtraction of the instrumental broadened FDD and the 750 K DMFT $E_{\rm F}$ weight, respectively.

(S.7) Other T-dependent measurements

Other experimental spectroscopy and scattering measurements of $CeCoIn_5$ also support and complement the ARPES and DMFT observations of f-c hybridization extending to much higher than T^*.

Optical. Early optical spectroscopy of $CeCoIn_5$ (12) observes signatures of a hybridization gap up to and *beyond* T^*, i.e. a 5-10 meV direct transition spectral dip that gradually fills in from 10 K to 100 K ($2T^*$), but continued spectral evolution including spectral transfer to higher energy is evident even between 100 K and 300 K. This result has recently been recognized (13) to be in conflict with early two-fluid model predictions of f-c hybridization occuring only below a temperature T_L ($<T^*$). This result has motivated an updated two-fluid model discussion involving the introduction of a new concept of "collective hybridization" or "lattice enhanced hybridization" (13) allowing for an extension of the predicted f-c hybridization regime up to T^*.

STM. Scanning tunneling microscopy (STM) and spectroscopy (STS) has also measured a hybridization gap on the Ce-In terminated surface in the temperature range 20 K to 70 K (14). Consistent with the optical spectroscopy, the hybridization gap dip in the averaged STS spectra becomes shallower at higher T but is still very much present at 70 K ($\approx 2T^*$) in comparison to $CeRhIn_5$ reference STS spectra. Similarly a narrow peak at E_F is observed in the averaged STS spectra on the Co-terminated surface, and the amplitude of this "f" state decreases to only 35% at 70 K, a large non-zero value consistent with the ARPES results in Fig. 4f. Two additional analyses of the T-dependent width and E/T power law scaling of this STS "f" peak are claimed to show signatures of quantum criticality as further discussed in Section S.13.

RXS. Recently resonant (elastic) x-ray scattering has demonstrated for the first time a q-dependent resonant enhancement sensitivity to bulk f states at the Ce $3d$-$4f$ M_5 edge (15). The RXS enhancement over a broad q-vector range of 0.2-0.4 ($2\pi/a$) along (110) is comparable to STM-QPI band visualization on the Co-terminated surface and both suggest scattering sensitivity arising from FS nesting between the 3D k_z-dispersive lobes of β FS sheet. The T-dependence of this (110) M_5-edge peak area, compared in Fig. S7 to the ARPES f-amplitude, exhibits a logarithmic dependence (linear on the log (T) plot) with the resonant enhancement persisting up to 150 K ($\approx 3T^*$). The RXS f-weight inherently goes to zero at 200 K because that spectrum was used as the baseline for background subtraction. The small RXS changes between 150K and 200K, leading to the choice of 200K as the baseline, may be related to the statistical noise floor of the experiment, in a similar manner that the weak f-enhancement in the ARPES α-band dispersion limited our analysis of its T-dependence to <100 K. Since the ARPES f-amplitude data also exhibits an approximate logarithmic dependence above 40K, alternative assumptions for the RXS or ARPES background subtractions, would enable a match between experiments. The RXS measurement would not be subject to the ARPES resolution amplitude suppression at low T.

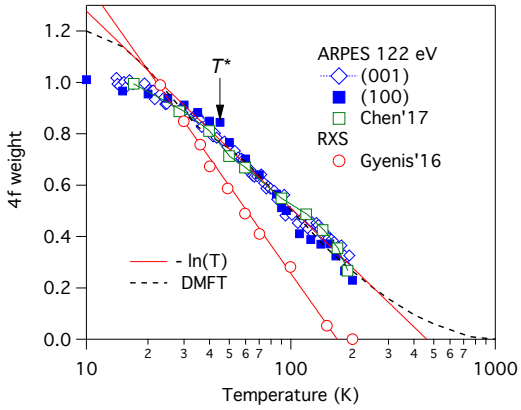

Fig. S7. Comparison of T-dependent resonant elastic x-ray scattering (RXS) f-area (15) and ARPES (001) and (100) surfaces hotspot $4f$-amplitudes to logarithmic profiles and to the DMFT profile (dashed). Scaled data points from Chen $et\ al.$ are also included, showing consistency between the two ARPES experiments.

ARPES. A recent purely experimental ARPES result on $CeCoIn_5$ by Chen *et al.* (16) presents similar T-dependent resonant-enhanced f-weight and dispersion results, combined with bulk-sensitive soft x-ray 3D FS measurements. Here we provide some commentary on the differences between Chen *et al.* and the combined ARPES-DMFT study reported here.

(i) Chen *et al.* report observation of multiple square-like FS sheets centered at the Z-point from soft x-ray ARPES using photon energies greater than 480 eV. The low photon energy ARPES results reported here provide a more detailed characterization of the complex Z-centered hole-like FS topology with comparison to DMFT, as discussed in Fig. 2 and Fig. S2.

(ii) Chen *et al.* provide an analysis of the resonant f-spectral weight peak *area* after subtraction of a higher-binding energy background level. We choose a different f-*amplitude* and Fermi-Dirac function background subtraction methodology to compare to DMFT calculations to avoid specific artifacts as discussed in Fig. S6. While the overall Chen *et al.* f-weight T-dependence is non-linear, they propose a *linear*-fit for 90 K to 190 K data points to extrapolate to zero amplitude to discuss an *onset* of f-c hybridization at $T{\sim}275$ K. Actually the Chen *et al.* f-weight scales well to the ARPES (001) and (100) analyzed here, as shown in Fig. S7, including the (energy resolution) amplitude suppression at lowest T, and an artificially suppressed amplitude at the highest T due to the choice of a high-binding energy background subtraction. Also the DMFT calculations exhibit a high T tail to the f-spectral weight evolution up to 1000 K that is not consistent with any extrapolation of <200 K behavior.

(iii) Chen *et al.* provide an analysis and estimate of FS volume changes of α and γ sheets to be a net increase of a small value of only 0.2 electron at 17 K relative 145 K, leading to a claim of "partial itineracy" at low T as compared to the theoretically expected incorporation of 1 electron between fully localized and fully itinerant Fermi surfaces. Indeed the DMFT plot of the T-dependent FS occupation in Fig. 5f increases by one electron from n_{FS}=3 to 4 electrons between 1000 K and 10 K, but only a net change of ∼0.6 electron change is predicted between 200 K and 20 K, reflecting an unanticipated 0.3 electron evolution of the FS volume above 200 K via k_F-shifts of the light effective mass conduction band, e.g. beyond the presence of an f-c hybridization dispersion kink. Thus the 0.4 electron difference in the low T f-participation in the FS may reflect critical underestimations in FS changes arising from (i) experimental resolution (15 meV) induced underestimates of the true k_F-crossing values, (ii) neglect of the contributions from the γ_Z and β' FS sheets newly elucidated here, and additional β FS sheet contribution arising from its larger effective mass. In particular, the edge of the γ_Z FS is shown in Fig. 4b to exhibit strong T-dependent f-weight reflective of changing f-participation in its FS. Also, the large effective mass effect on the low T k_F-shift for the β band is dramatically highlighted along one particular X-M cut in Fig. S9, and also persists when averaged over the entire Γ-plane FS orbits as discussed in Fig. S11.

(iv) Chen *et al.* report observation of a narrow-width second-excited CEF peak at 25 meV at temperatures as high as 145 K employing division by a resolution-convolved Fermi-Dirac distribution (RC-FDD) function. Due to the theoretical T-dependent broadening of this CEF peak above 90K, this result is not reproduced when performing the same RC-FDD spectral recovery procedure on the DMFT spectral function as explored in Section S.12.

(v) Chen *et al.* analyze the width of the Fermi level f-peak and also E/T scaling over temperature ranges similar to the STM/STS analyses, but reach different conclusions than Aynajian *et al.* regarding the relation of observed T-linear dependence of the width and "*intermittant*" scaling to quantum criticality as further discussed in Section S.13.

(vi) Chen *et al.* use Fermi-level spectra divided by a resolution-convoluted Fermi-Dirac distribution under different polarizations of the incident x-rays and symmetry arguments to claim experimental identification of the energy ordering of the CEF states as Γ_7^+, Γ_6 and Γ_7^-. This is counter to the DMFT prediction of the energy order of the CEF states with Γ_6 being the highest energy state, and to x-ray absorption and neutron studies that similarly claim a pure J_z=1/2 second excited state (17). The authors revert back to the more standard energy ordering of CEF states when discussing ARPES results for $CeIrIn_5$ (18).

k/q-selectivity. The STM-QPI and RXS scattering measurements provide very selective k-space views of the f-c hybridization, with scattering q-vector selectivity highly dependent upon favorable FS nesting conditions and with ill-defined k_z-dependence. Another STM study attempted to derive a low T FS of $CeCoIn_5$ solely from the QPI analysis (19), but the resulting FS contours show significant shape and size discrepancies with DFT calculations and with the ARPES and DMFT reported here. In contrast, the 122 eV resonant ARPES highlights enhanced f-character in a k-selective two-dimensional cut through the bulk BZ as shown in Fig. 1e, and with additional orbital symmetry selectively from the polarization of the incident light. Nevertheless, the ARPES identification of three FS locations of f-character enhancement using two orthogonal (001) and (100) cleave surfaces is also incomplete. Another likely location of enhanced f-weight, previously noted in Fig. 1d as a secondary scenario #3, is the shallow electron pocket along the R-Γ diagonal. However, the resonant ARPES condition for the two cleave surfaces misses cutting through this FS feature. Non-resonant ARPES of dispersion kink signatures of f-c hybridization are also observed in $CeCoIn_5$ and in principle have less k-selectivity restrictions with possible improved energy and momentum resolutions, but the inference of f-character and characterization of its T-dependence can be more challenging.

(S.8) Two-fluid model

The phenomenological two-fluid model (20, 21) postulates a relative T-dependent weighting between a "heavy" Kondo liquid that develops from the *collective* hybridization of conduction electrons with the localized f-moments below the lattice coherence temperature T^*, and a "light" Landau Fermi liquid that results from the conduction electrons that do not hybridize with the localized moments. This model of "partial" condensation is conceptually consistent with the Kondo cloud schematics shown in Fig. 1b in which *partial* f-moment screening exists throughout the T regime between ${T_K}^{gs}$ and ${T_K}^{onset}$, and *partial* lattice coherence between ${T^*}_{gs}$ and ${T^*}_{onset}$.

A proposed universal scaling formula for the f-quasiparticle spectral density of states (DOS):

$$\rho_{KL} = (1 - \frac{T}{T^*})^{3/2}(1 - ln\frac{T}{T^*}) \quad [1]$$

codifies the two-fluid model prediction of *collective* f-c hybridization of conduction electrons to the localized f-moments below T^*(8). This scaling formula has two multiplying **"hybridization order parameter"** and **"effective mass"** terms, where the first term goes to zero at T=T^* and the second logarithmic term goes to zero at a higher temperature of $T = e{\cdot}T^* \approx 2.7$ T^*. A comparison of the T-dependences of the individual components of this two-fluid universal f-DOS scaling function and their multiplication for T^*=50 K, with normalization to unity at 5 K, is plotted in Fig. S8a.

Since the two-fluid f-DOS scaling formula does not contain any of the previously described effects of E_F versus KR peak T-profiles, the CEF tail or degeneracy crossover effects, or experimental resolution suppression of low T amplitudes, we have limited expectations for agreement with ARPES or DMFT T-profiles that include CEF effects. Previously the DMFT-calculated quasiparticle f-DOS of the Kondo resonance peak amplitude for $CeIrIn_5$ (22), without the inclusion of CEF states, was favorably compared to the two-fluid universal scaling function using $T^* \approx$ 31 K (13, 23). However, a high T offset was necessary to apply to the DMFT result to obtain the favorable comparison. A similar comparison to the DMFT $CeIrIn_5$ KR peak amplitude (22), without any background subtraction or offset, is also provided in Fig. S8a, where the discrepancy in a non-zero high T tail above 100K is evident.

The much larger discrepancy between the two-fluid formula (using T^*=50 K) and the current DMFT KR peak amplitude for $CeCoIn_5$ including CEF effects, is shown in Fig. S8b. A much larger T^* parameter of $\approx$ 400 K is required to best match the intermediate region of the DMFT KR T-profile, with normalization to unity at 10K. The near logarithmic behavior of the DMFT profile in the intermediate 20-140K regime is also shown in Fig. S8b.

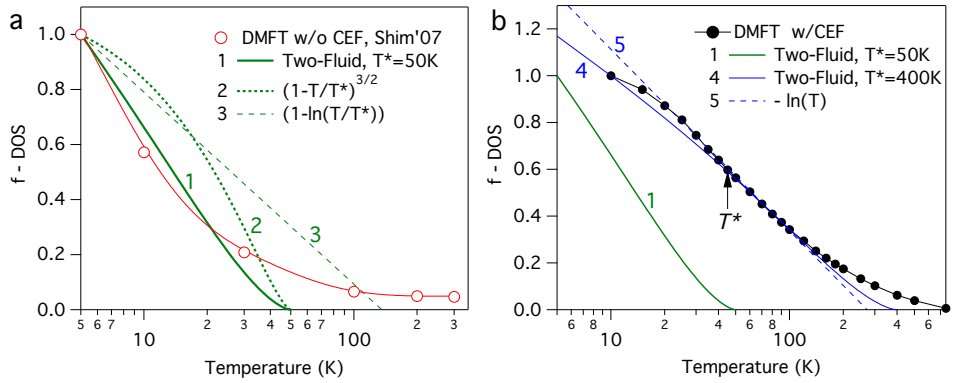

Fig. S8. (a) Comparison of the two-fluid model universal scaling formula with T^*=50 K, and its two multiplicative terms to the T-dependent DMFT Kondo resonance peak amplitude profile without inclusion of CEF states (from (22)). **(b)** Comparison of the T-dependent DMFT Kondo resonance peak amplitude profile (including CEF states) to the two-fluid model scaling formula for T^*=50 K and 400 K, and to a logarithmic dependence in the 20-150 K region.

(S.9) β-band dispersion analysis

Figure S9 expands on the main text presentation of the α band dispersion and quantitative analysis of the $k_{\rm F}$ and $v_{\rm F}$ in Fig. 3 to include comparison to the heavier β band dispersion. The β-band is observed to have an $\sim$2$\times$ larger $\Delta k_{\rm F}$-shift and $\sim$10$\times$ smaller $v_{\rm F}$ than the α-band at low T. Estimation of the effective mass from $m^* = 7.62 k_F$ [Å^{-1}] / v_F [eV-Å], thus also gives an order-of-magnitude larger $m^* \approx 180$ for the β-crossing as compared to $m^* \approx 15$ for the α-crossing. The large FS volume of the β sheet combined with large T-dependent $\Delta k_{\rm F}$-shifts is suggestive that the β sheet FS volume change will be the dominant contribution to the total FS volume evolution plotted in Fig. 5f.

The transport coherence temperature T^* appears to be associated with the maximal rate of change of the β-band dispersion quantities, more so than for the α-band T-dependence, where T^* is closer to its low T saturation. This could be due to the close-proximity effect on the α-band in this Γ-plane X-M cut. The relative proximity of α, β (and γ) FS sheets in $CeCoIn_5$ varies throughout the BZ, and hence the relative effective masses of these sheets will be strongly k-dependent. The effective mass measured by dHvA quantum oscillations will reflect an *average* over these these large local k-point m^* variations. The close proximity of the β and γ bands to each other near to the zone center along Γ-M has been previously discussed in terms of the need for a three-band hybridization model to simulate observed on-resonance ARPES f-weight (24).

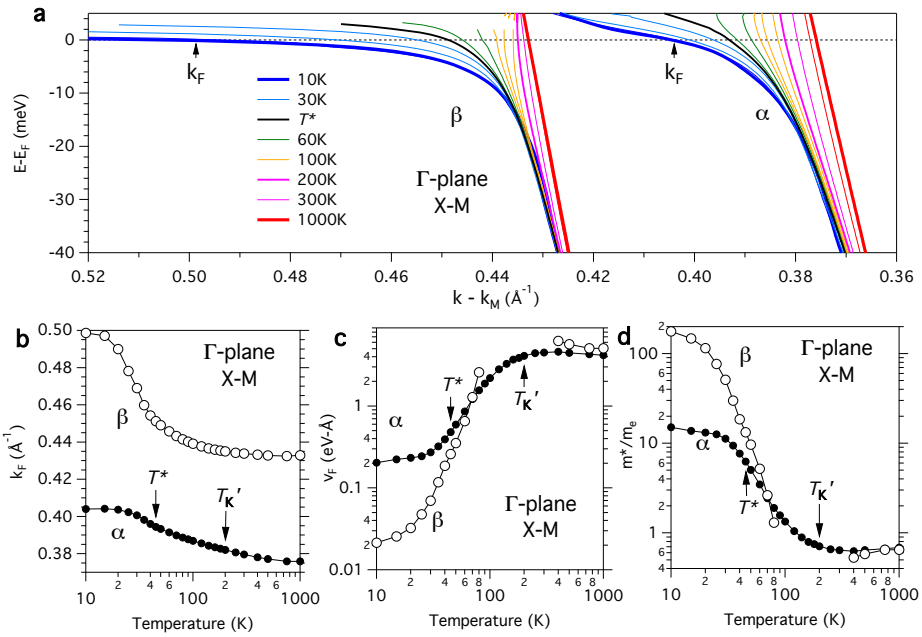

Fig. S9. (a) DMFT T-dependence of both α and β band dispersion along X-M in the Γ-plane. **(b-d)** Quantitative analysis of (**b**) the Fermi momentum, (**c**) the Fermi velocity, and (**d**) the effective mass (=7.62 $k_{\rm F}/v_{\rm F}$).

(S.10) k-resolved CEF degeneracy crossover

To complement the k-integrated CEF degeneracy crossover merging of the two lowest CEF f states in Figs. 5(d) and 5(e), k-resolved spectral functions along X-M for three select low temperatures are shown in Fig. S10. Note that by 50 K ($\approx T^*$) the two lowest CEF f-states have merged and are indistinguishable, while clear heavy mass dispersions of β and α-band near $E_{\rm F}$ are still visible consistent with Fig. S9 analyses.

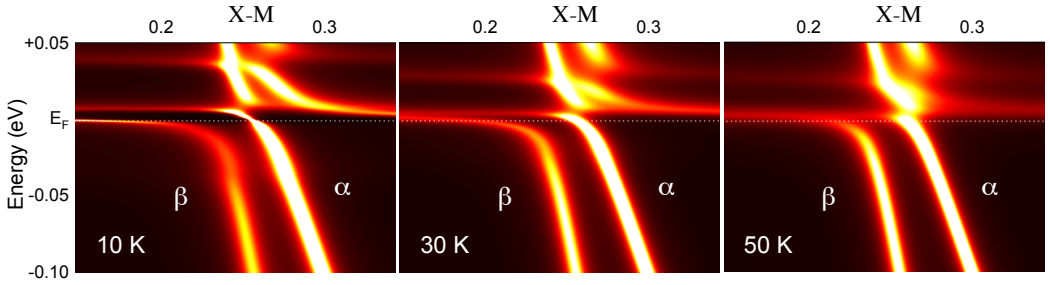

Fig. S10. DFT+DMFT k-resolved β and α-band crossing spectral functions along X-M for three temperatures from 10 K to 50 K ($\approx T^*$) showing the CEF-merging degeneracy crossover effect.

(S.11) DMFT comparison to dHvA

The DMFT calculated T-dependence of the α and β sheets can alternatively be analyzed in terms of the momentum space *area* enclosed by k_F, similar to how experimental de Haas-Alphen (dHvA) quantum oscillations measure the FS orbit size. Fig. S11a shows the DMFT "small" to "large" FS transition from analysis of the Γ-plane α_2 and β_1 FS cross-sectional areas. The area results are plotted with conversion to both dHvA frequency (left axis) and also to the average k_F values (right axis) assuming a circular orbit. The *average* k_F values for α_2 (β_1) are naturally smaller (larger) than the *specific* k_F values along X-M plotted in Fig. S9 due to the non-circular diamond (flower) shape of the α (β) FS contour in the Γ-plane. Similar to the Fig. 5f plot of n_{FS}, the coherence temperature T^* is observed to be in the middle of this "small" to "large" FS transition. For comparison to experimental dHvA, "itinerant" $CeCoIn_5$ dHvA (001) frequencies (25) are used for the low T comparison and "localized" $LaRhIn_5$ (26) dHvA (measured below T = 40 mK) are used for the high T comparison to DMFT. Decent overall agreement is found between the DMFT calculation and dHvA results, especially for the β orbit. Also the "localized" $LaRhIn_5$ dHvA finds better agreement to the highest 1000K DMFT values.

The DMFT calculation exhibits an almost 2× larger relative change in the β_1 FS (18%) as compared to the α_2 (11%) as illustrated in Fig. S11b with normalization to T=1000K. Normalization of each DMFT profile to the experimental ARPES maximum temperature of 200K also shows an enhanced relative FS change for the β_1 orbit. Such enhanced relative change in FS size for the heavier effective mass β_1 FS sheet, if significant when averaged over the entire FS, may be an important factor for the ARPES-based quantitative estimation of the β contribution to the f-participation in the FS as attempted by Chen *et al.* (16) (see discussion in Section S.6).

In contrast, the experimental dHvA frequency difference between $CeCoIn_5$ and $LaRhIn_5$ for the α_2 orbit is ∼2× larger than the DMFT calculation for $CeCoIn_5$, and thus both α_2 and β_1 have similar 20% relative FS changes. This theory-experiment discrepancy could reflect an incorrect assumption that $LaCoIn_5$ accurately represents high temperature $CeCoIn_5$.

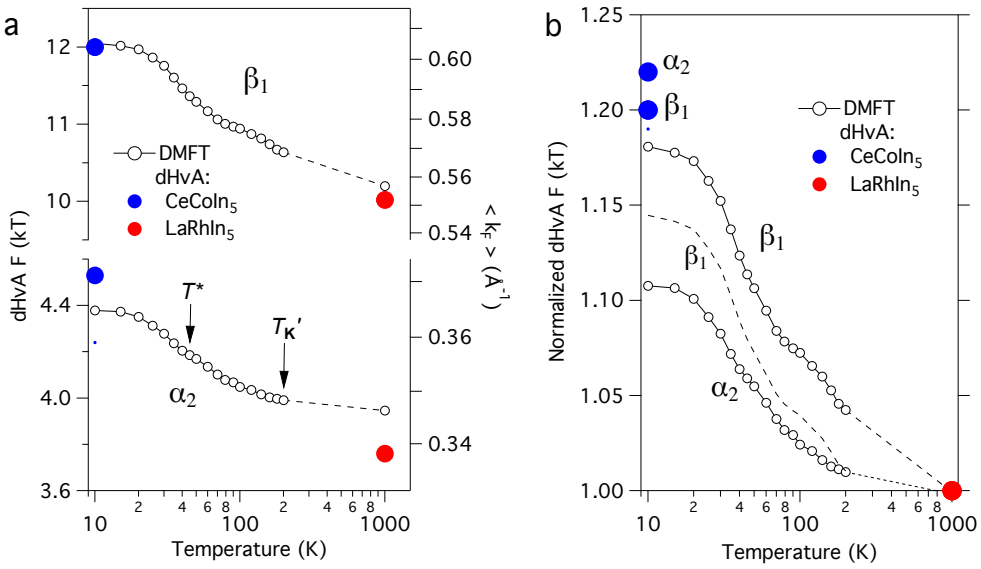

Fig. S11. (a) T-dependence of the DMFT α_2 and β_1 Γ-plane cross sectional areas (converted to dHvA orbit frequency and average Fermi momentum, k_F) with comparison to dHvA FS orbits at low T to "itinerant" $CeCoIn_5$ and at high T to "localized" $LaRhIn_5$. **(b)** dHvA frequencies normalized to high T values illustrate a relatively larger change in the DMFT FS area of the β_1 orbit compared to the α_2 orbit, both for scaling to 1000K and to 200K (dashed line).

(S.12) Recovery of f-states above E_F

The narrow peak at E_F in photoemission in Kondo systems reflects the relative small occupied tail of the Kondo resonance which is comprised of strong narrow f peak(s) in the meV-range just above E_F, including CEF splittings. It is desirable to try to quantitatively recover information about these spectral peaks from the thermal excitations that contribute to the measured spectral lineshape above E_F. Starting with a known full spectral function $A(\omega, T)$, the measured photoemission spectrum S reflects the multiplication of the Fermi-Dirac distribution (FDD) function followed by a Gaussian convolution (GC) with energy resolution width ΔE, e.g. steps performed to the k-integrated DMFT calculation in Fig. 5: $S = [A(\omega, T) \times \text{FDD}(T)] \circ \text{GC}(\Delta\text{E})$. A common approximate one-step recovery procedure is to divide the experimental spectra by a resolution-convolved Fermi Dirac distribution function (RC-FDD), i.e. $A' \approx S \,/\, [\text{FDD}(T) \circ \text{GC}(\Delta\text{E})]$.

For high temperature where ΔE is less than the FDD thermal broadening width ($\approx 4k_BT$), the approximation is good. However for low temperature where ΔE is larger than $4k_BT$, the approximation breaks down, as illustrated in Fig. S12 where the RC-FDD division recovery is attempted for simulated "experiments" with energy resolutions of 5, 10 and 15 meV. With the original DMFT spectral function (A) in Fig. S12a as a reference, it is observed that below the T=ΔE/$4k_B$ lines, the recovered spectral function (A') is progressively shifted to higher energy as the instrumental broadening dominates more over the increasingly narrower intrinsic FDD linewidth at lower T. Also reflected in the A' images in Fig. S12b-d is an unrecoverable region where numerical noise sets in beyond $\approx 10k_BT$ above E_F.

The failure of the approximate RC-FDD division method to accurately recover the original spectral function is also illustrated for 10K, 30K and 60K spectral lineshapes in Fig. S12e-g for the three instrumental broadenings. The ability to resolve the first CEF excitation at 8 meV is not possible even for 5 meV resolution in part because the degeneracy crossover into a single merged Kondo peak occurs already by 30K. While the theoretically predicted low T energy shift of the second CEF peak from 40 to 25 meV resides entirely in the inaccessible $>10k_BT$ region, the ability to recover this peak at $\approx$25K is limited to a narrow T window above ΔE/$4k_B$ for ΔE=5 and 10 meV before it becomes too broad to distinguish. Experimentally these regions are also not accessible due to statistical noise that limits the recovery typically to $<5k_BT$ (11). This is illustrated for the addition of 1% Gaussian noise to the T=30K simulation in Fig. S12f and to the 5 meV resolution "experimental" S spectra before the RC-FDD division step in the Fig. S12h image.

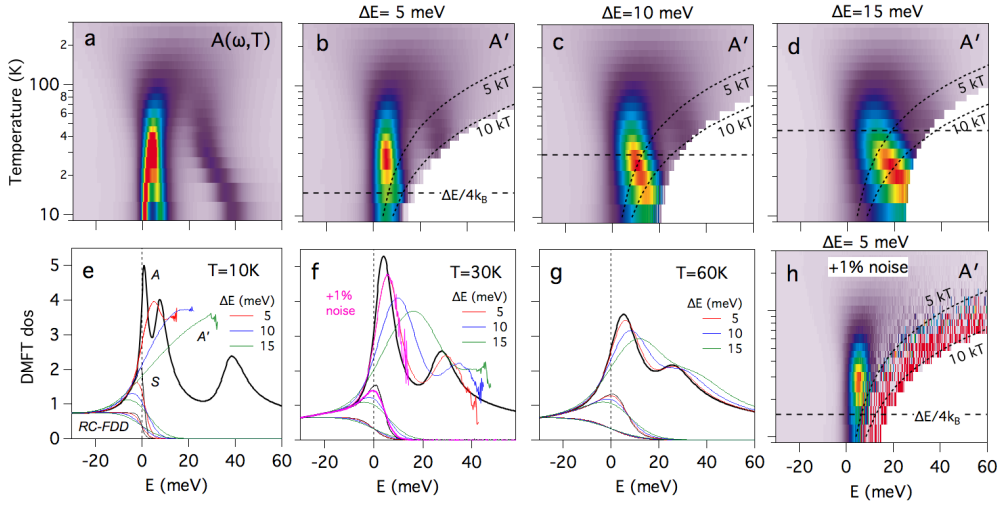

Fig. S12. (a) T-dependent DMFT spectral function for $CeCoIn_5$. **(b-d)** Recovered T-dependent spectral function A' using RC-FDD division for instrumental broadenings of 5, 10 and 15 meV. **(e-g)** Recovered spectral lineshapes for varied instrumental broadening for T=10, 30 and 60K. **(h)** Recovered T-dependent spectral function A' including Gaussian simulated statistical noise added to the spectrum S before division by the RC-FDD.

Hence we conclude from this exercise of using the theoretical k-integrated DMFT spectral function for $CeCoIn_5$, that we are not able to reproduce the experimental analysis claims of Chen *et al.* (16) of using the RC-FDD division method to recover (i) a few meV centered Kondo peak, (ii) observe its centroid shift to 8 meV above 60K, and (iii) observe the 25 meV second CEF level above 90K. The RC-FDD division procedure is also well known to be very sensitive to meV-level changes in the E_F-calibration of the spectra S, and to small background offsets applied to the RC-FDD to control the mathematical divergence. Other artifacts in the recovered lineshape A' can be generated by mismatching of parameters between the creation of S and in the RC-FDD function, including some compensatory effects that can artificially get the energy centroid correct, but at the expense of amplitude and width. Nevertheless, even if the RC-FDD method is quantitively inaccurate in the important low T regime for most Kondo systems, it is still a useful procedure for normalizing the intensities above E_F for visualization of k-dependent or polarization-dependent changes of the KR and CF_1 intensities. An example in this work is the visualization of a 30K thermally-occupied γ band hole pocket hotspot above E_F at the CF_1 energy in Fig. S2e.

(S.13) Quantum criticality

The M-alloy phase diagrams of the Ce-115 family of compounds CeMIn$_5$, where M=(Co,Rh,Ir), exhibit multiple magnetic quantum critical points (QCP) owing to CeRhIn$_5$ having an anti-ferromagnetic ground state, while CeCoIn$_5$ and CeIrIn$_5$ are low T superconductors. Quantum critical fluctuations may extend to relatively large energies and temperatures and produce characteristic behaviors within a fan of proximity near the singular QCP (27). One such characteristic behavior of T-linear resistivity observed in CeCoIn$_5$ from T_c up to about 20K is thought to be a signature of quantum criticality reflecting its proximity to the Ce(Co,Rh)In$_5$ QCP. Similarly, the resistivity of CeIrIn$_5$ possesses a non-Fermi liquid $T^{1.3}$-dependence. Hence in spectroscopic measurements of Ce115s, one test for critical behavior is to look for similar T-linearity in the scattering rate of the heavy quasiparticles from measurement of the width of the Fermi-level Kondo resonance peak. A second test of criticality specific to the physics of Kondo destruction is to look for E/T scaling of the T-dependent lineshape of the Kondo resonance peak. Analysis of both criticality tests have recently been performed on CeCoIn$_5$ by scanning tunneling spectroscopy (14) and by ARPES (18).

Scattering rate. The Aynajian *et al.* **tunneling** measurement of this T-dependent quantity focused on extraction of the peak parameters from a narrow STS "f" peak found on the B-type (Co-terminated) surface in the T range of 20K to 70K. Processing steps included (i) subtraction of a sloping background, (ii) a three-peak fitting analysis constrained to the best fit peak energies of the sharpest 20K STS spectrum, and (iii) correction for a thermal broadening contribution from raw FWHM fit values. While the raw FWHM fit values exhibit a non-linear dependence (e.g. power-exponent ≈0.7), the authors are able to rationalize a linear fit within the error bars that increase to higher temperatures where the broader peaks overlap more.

Aynajian *et al.* specifically attempt to correlate their T-linear scattering rate above 20K to the T-linear resistivity of CeCoIn$_5$ below 20K with the implicit assumption that the STS peak width linearity extends below their minimum measurement temperature. E.g. the STS minimum FWHM value of ≈11 meV is (thermal broadening) corrected down to ≈7 meV and the linear fit extrapolation to T=0 gives a finite 3.5 meV width, which is interestingly in rather good agreement with the DMFT peak width of 3.2 meV at 10K (see Fig. 5e).

The Chen *et al.* **ARPES** experimental extraction of the Kondo resonance width at a specific Γ k-point at 122 eV involved steps of: (i) division by the spectra by the T-dependent RC-FDD (whose artifacts are describe in the previous Section S.12), (ii) quantification of the occupied-side leading edge half-width with (iii) minor correction at higher T from the influence of a second CEF state, and (iv) correction for a 17 meV experimental energy resolution broadening. In this case, the minimum quantified FWHM of ≈22 meV at 17K is corrected to 15 meV, and the T-linear extrapolation to T=0 gives a 12 meV intrinsic width value, i.e. a distinctly larger value than obtained by STS or DMFT. The authors do not explicitly speculate a correlation of their k-selected T-linearity above 17K with the k-integrated T-linear resistivity of CeCoIn$_5$ below 20K.

The **DFT+DMFT** calculations presented here inherently do not reflect any two particle correlations such as magnetic fluctuations (cluster DMFT would be required) and hence signatures of quantum criticality are not expected. Nevertheless, in the spirit of our T-dependent f-amplitude treatment of the DFT+DMFT theory to compare to experiment, it is instructive to perform a similar leading edge half-width analysis of the k-integrated DMFT spectral function presented in Fig. 5. The result, plotted in Fig. S13c, interestingly *does* show a uniform power law T dependence very close to linearity from 40K to 200K, with small deviation to a sub-linear power law exponent of 0.85 below the first CEF degeneracy crossover into the regime of the T-linear transport.

E/T scaling. The generalized power law scaling mathematical treatment of a T-dependent spectral lineshape involves plotting the lineshape in question with an amplitude rescaled by T^{α} versus a rescaled abscissa of $(E/T)^{\beta}$, and looking for the collapse to a universal curve for specific exponent values. The separate α amplitude exponent is single purpose, while the dual purpose β exponent simultaneously controls *both* the energy centroid and width of the rescaled lineshape. If any one of the three lineshape quantities deviates from a power law scaling, or the centroid and width obey different β exponent scalings, then the collapse to a universal curve fails.

The Aynajian *et al.* **tunneling** E/T scaling analysis of the STS B surface "f" peak again involved a background subtraction of each spectrum, but without the multi-peak fitting or thermal broadening correction steps used for the peak width analysis. A systematic variation of α=0.4-0.7 and β=0.5, 1.0, and 2.0 was explored to obtain the best lineshape collapse for α=0.53 and β=1.0 for the T-range of 20 - 60K. The lowest temperature 20K scaled lineshape has the greatest deviation from the collapse of the other four temperatures and a higher 68K STS spectrum is not included in the scaling analysis. The authors specifically claim this E/T scaling result is a signature of the quantum criticality of CeCoIn$_5$.

The Chen *et al.* **ARPES** E/T scaling analysis of the specific Γ-point resonance spectra similarly forgoes the peak width analysis steps of division by the RC-FDD function, and no background subtraction step is evident. The authors present a final scaled result of five spectra from 30K to 90K specifically for β=1 and with best intensity scaling for α=0.36. The binding energy depth of the collapse of the tail lineshape decreases from -1 eV to -0.5 eV as the low energy background of the scaled lineshape rises at higher T due to the existence of a higher binding peak (e.g. SO′) in the ARPES spectra. Perhaps due to

this effect the authors characterize the result as "*approximate*" E/T scaling. Most significantly, the lowest 17K and highest 120K spectra are shown to fail to scale with the other intermediate temperatures. Thus the authors also describe the result as "*intermittant*" E/T scaling, and conclude thereby that it must be unrelated to the T-linear resistivity below 20K or quantum criticality – a very different conclusion from the STM claims. Instead the authors speculate that the apparent scaling may be related to the thermal depopulation of excited CEF levels at lower temperature.

First we explore the generic effects of background offsets and energy resolution on the amplitude scaling of a **model Lorentzian function**, $A(\omega,T) = (a_0/T)/[(\omega - e_0T)/(w_0T))^2 + 1]$ with inherent E/T scaling. Coefficients $a_0 = 0.1/k_B$, $w_0 = 20k_B$ and $e_0 = 5k_B$ are chosen to be in the range of the ARPES experiments, e.g. 10-100 meV width and energy variation, and ~1 to 10^{-2} amplitude reduction over T=5-750K, as shown in Fig. S13b. The power law analysis of this function shows straight lines in the log-log plots of Fig. S13a, as expected, corresponding to α=β_w=β_e=1.

The effect of adding a small background offset (b) to $A(\omega,T)$ is that instead of scaling towards zero, the amplitude approaches a constant at high T (α→0), illustrated for (b=0.05, 0.1, 0.2 and 0.4). The effect of energy resolution broadening is that the amplitude (and width) saturate to a constant value at low T (α, β_w→0), illustrated for ΔE=15, 30, 50 meV. The combination of the two effects with deviations at both low and high T is that an intermediate T range exhibits "approximate" amplitude scaling with a reduced α exponent. For 15 meV energy resolution broadening and b=0.1 and 0.2 offsets, the effective amplitude exponents are α≈0.5 and 0.35, respectively. Hence independently of the actual β-scaling behavior, we can propose a natural explanation for the observation of the "*approximate*" and "*intermittant*" E/T scaling in ARPES by Chen *et al.*, and propose that the different α exponents between tunneling and ARPES come from differing background subtraction methods.

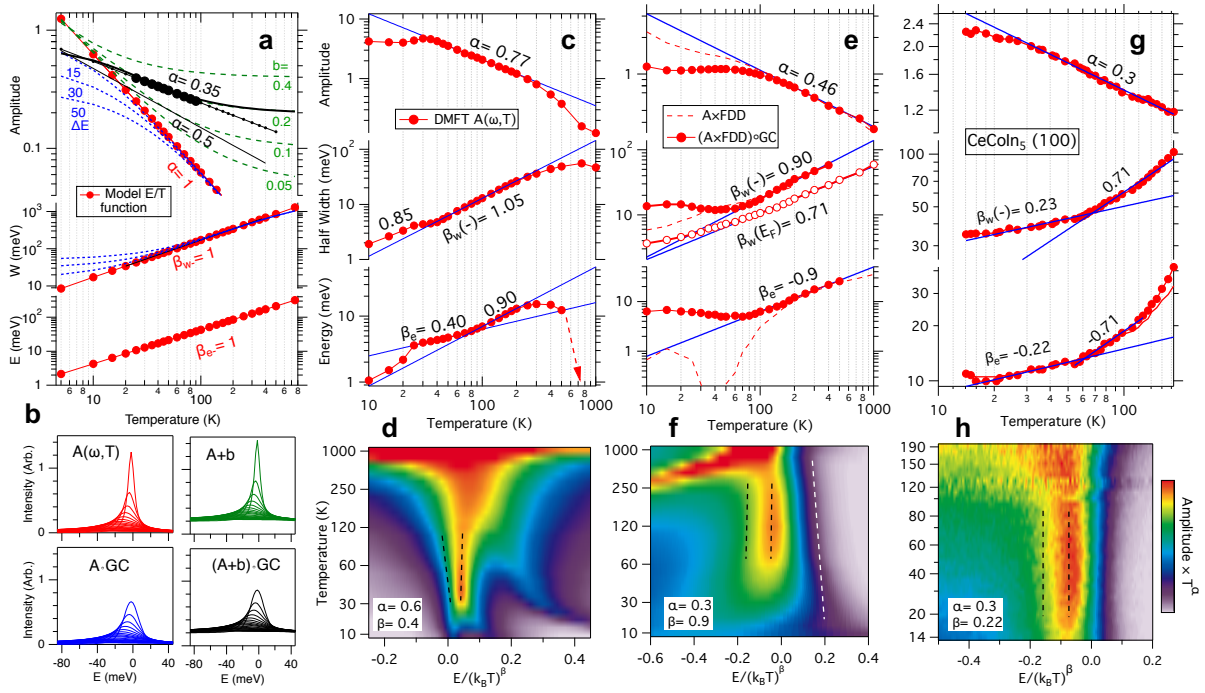

Fig. S13. **(a)** Power law analysis of the peak amplitude, width and energy of a model Lorentzian function with inherent E/T scaling, and with modification by background offsets and energy resolution broadening, visually illustrated in the panels in **(b)**. **(c)** Power law analysis of the full k-integrated DMFT spectral function for $CeCoIn_5$ showing effects of the complexity of the CEF T-dependence. **(d)** Image representation of the power law scaled image of the DMFT spectral function for β=0.4 which best scales the peak energy in a limited T range of 25-60K. **(e)** Power law analysis of the DMFT spectral function multiplied by the Fermi-Dirac cutoff and energy resolution broadened to simulate the photoemission experiment. **(f)** Power law scaled image of the DMFT "photoemission" spectra for β=0.9 which simultaneously scales the peak energy and leading edge width in a T range above 60K, while overscaling the width above E_F which obeys a different β scaling. **(g)** Power law analysis of the experimental $CeCoIn_5$(100) ARPES f-hotspot, exhibiting different low and high T regime β scalings. **(h)** Power law scaled image of the ARPES data for the low T regime with small β=0.22 exponent.

Next we analyze the power law scaling of the full theoretical **DMFT spectral lineshape** to explore effects of the complexity of the asymmetric lineshape with shifting and merging CEF peaks above E_F. Indeed the first CEF degeneracy crossover at ~30K creates a distinct signature in all three profiles in Fig. S13c, amplitude, leading edge peak width and energy. As noted earlier, the low energy leading edge half-width does exhibit a nearly T-linear scaling exponent of β=1.05 in a large T range above 40K. The profile of the energy of the peak maximum has a much slower β=0.4 T-dependence just above the first CEF crossover and then increases to β=0.9 with the merging of the second CEF level, before non-monotonically shifting to lower values and below E_F for the extreme high T broadening. Hence the conditions for power law scaling of all three quantities is limited to 70-200K. The lower T regime with discrepant ($\beta_e \neq \beta_w$) scaling is illustrated in an image plot representation for scaling with β=0.4.

Multiplication of the DMFT spectral function by the FDD(T) cutoff radically changes the peak energy variation to be mostly negative (towards high binding energy) but still with a non-monotonic positive shift to being above E_F around 40K (dashed line in Fig. S13e). Convolution with an instrumental energy resolution of 15 meV masks out this fine energy scale behavior, as it exhibits the same low T effects ($\alpha, \beta_w \rightarrow 0$) as described for the model function. Above 70K, the peak amplitude scaling has been reduced from α=0.77 to 0.46 due to the FDD function cutting off the main Kondo resonance peak, and the resolution broadening has also reduced the half-width exponent to become equal to the energy scaling (β_w=β_e=0.9), enabling a near T-linear scaling in this regime as illustrated in Fig. S13f.

For large β scaling exponents close to 1, additional high binding energy peaks such as the ∼0.3 eV SO′ sideband excitation are progressively scaled into the regime of interest at higher T as seen in Fig. S13f, and also experienced in the Chen *et al.* E/T ARPES scaling. Also noteworthy is that E/T scaling is not observed for energies just above E_F. While the FDD function is inherently a function of (E/k_BT) and thus obeys β=1 power law scaling of its width, it is only for constant amplitude (α=0) scaling. Thus multiplication of the FDD to a lineshape with α>0 scaling will modify the Fermi-edge cutoff width scaling to $\beta \neq 1$.

Finally we analyze the power law scaling of one of the experimental **ARPES data sets** for $CeCoIn_5$, choosing the (100) surface γ_Z FS f hotspot from Fig. 5d. While the energy resolution broadening does not appear to fully saturate any of the three quantities in Fig. S13g, in contrast to the DMFT photoemission simulation, there appears to be two distinct low and high T regimes with 60K crossover, and equal width and energy scaling exponents in each regime, consistent with the DMFT simulation. The low T scaling regime with very small β=0.22 exponent extending up to 60K, illustrated in Fig. S13h, is in stark contrast to the Chen *et al.* Γ-point E/T scaling (β=1) between 30K-90K. Only above 60K does the β exponent rise to 0.71, still significantly smaller than near T-linear photoemission simulation. The amplitude scaling exponent for this measurement is reduced to a small value of α=0.3, consistent with the Chen *et al.* ARPES study employing no background subtraction.

(S.14) Dirac-like band crossing

Recently a Dirac-like band crossing along Γ-Z has been identified by Shirer *et al.* (28) in uncorrelated DFT calculations as a double degenerate point arising from the C_{4v} rotational symmetry of the c-axis (as well as inversion and time reversal symmetries). In the k_x-k_y plane, it is actually a quadratic band dispersion crossing point (QBCP), as shown in Fig. S14a for k_z=0.475(Γ-Z) for a $LaCoIn_5$ DFT calculation. Hence it is not a true bulk 3D Dirac point, which possesses linear band dispersions in all k-directions. A QBCP is known to be sensitive to gapping or splitting into pairs of Dirac points with breaking of the 4-fold rotational symmetry (29). The upper (lower) quadratic band has predominant Co $3d_{x^2\text{-}y^2}$ (d_{z^2}) character with secondary In(2)-s (In(1)-p_z) character. The degenerate band crossing point, resulting from the opposite $\Gamma_{3+}(B_{1g})$ and $\Gamma_{1+}(A_{1g})$ symmetry of the bands relative to the c-axis, is demonstrated by Shirer *et al.* to be a universal feature for La115 and localized f-core Ce115 DFT calculations. In addition, surface state arcs connecting the two crossing points per Brillouin zone are theoretically predicted for the (100) surface.

An open question in Shirer *et al.* is whether the Dirac-like feature and its topological implications will survive the Ce $4f$ electron correlations. Coincidentally, the 110 eV spectrum of ac-cleaved $CeCoIn_5$ in Fig. 2g, is the ideal Z-Γ-Z high symmetry cut to look for these DFT predictions in the presence of f-correlations. In Fig. S14b the two relevant ARPES bands are clearly visible with the γ band having stronger intensity and a narrower width continuous parabolic-like dispersion up to E_F. However, the weaker V-shaped γ_Z band dispersion exhibits a discontinuity between -0.2 eV and -0.1 eV, seemingly aligned to the γ band at *two* points. This more complex band crossing behavior and the clear absence of the predicted surface state (dashed line) within the bulk projected gap across Γ, suggests that the doubly degenerate crossing point and its topological implications do *not* survive in $CeCoIn_5$.

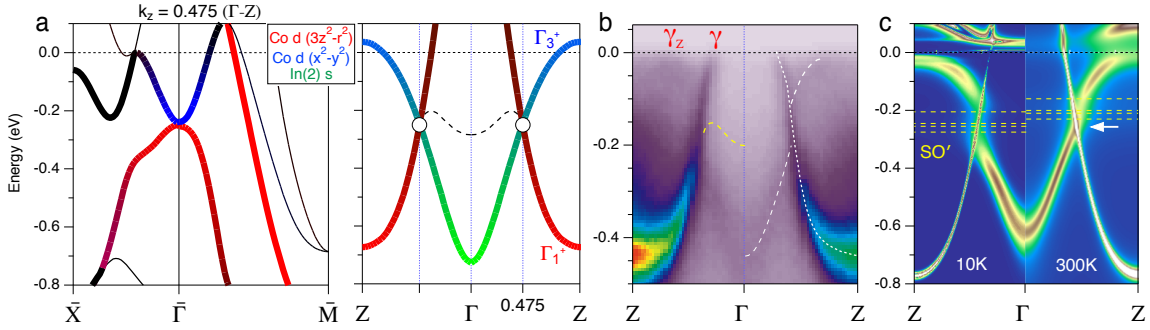

Fig. S14. (a) DFT band structure for $LaCoIn_5$ showing quadratic band dispersions in the k_x-k_y plane at the crossing point which is Dirac-like along k_z. Dominant Co d and In(2) s orbital characters are color-coded and band symmetry labels shown. A predicted DFT surface state (dashed) connects two crossing points. **(b)** ARPES band dispersion along Z-Γ-Z measured at 15K, with dashed guide to eye dispersions on one half and a schematic DFT surface state prediction (yellow dashed). **(c)** DFT+DMFT calculation for T=10K and 300K. At low T, the SO′ f-levels (dashed lines) hybridize with and disrupt one of the two bands at the crossing point energy. At high T, the SO′ hybridization weakens and shifts to higher energy allowing recovery of the Dirac-like crossing point (arrow).

To theoretically explore this complex behavior and discrepancy with uncorrelated DFT, we plot the low and high T correlated DFT+DMFT predictions for this $CeCoIn_5$ high symmetry cut in Fig. S14c. Visually, the 10K DMFT spectral function image reproduces quite well the 15K experimental measurement, including the γ_Z band discontinuity behavior. The theoretical understanding of the DMFT result is that there is a coincidental direct conflict of the spin-orbit sideband excitations (SO′ in Fig. S4), composed of four levels between -0.2 and -0.3 eV, with the Dirac-like crossing point energy. The SO′ levels provide symmetry-compatible hybridization with and ∼0.2 eV wide disruption of the γ_Z band, while the γ band remains non-interacting with both.

While general topological theory of scale invariance in the Dirac Fermion model predicts Coulomb interactions to be *marginally irrelevant* to the Dirac fixed point (30), we regard the disruption of the Dirac-like degenerate crossing point and absence of experimental surface states, as the result of the strong perturbative introduction of a *third* hybridizing band to the original two-band crossing problem, and not a weak indirect f-correlation effect on the crossing point. Since these extra interrupting bands have f origin (excitations of the SO-split Kondo resonance), we expect its coherent hybridization to diminish at high T. Indeed the 300K DMFT prediction in Fig. S14c shows this T-dependent weakening of the disruption of the γ_Z band, but not complete disappearance, consistent with the other demonstrations in this work of f-c hybridization well above T^*. In addition, the SO′ states shift ∼40 meV to higher energy, as also observed in Fig. S4, thereby allowing the crossing point to emerge just below the SO′ states.

Additional (100) surface Ce115 ARPES is required to further explore when the crossing point is able to survive the SO′ state disruption in order to verify the existence of surface states. Also the energy scale difference between ARPES and theory in the Fig. S14 comparison, reflects a bandwidth error for the α, β and γ bands that originates from additional d-electron correlations in the relatively narrow bandwidth of the Co $3d$ bands that are not treated in the DFT or DFT+DMFT calculations, and which are of lesser importance for the $4d/5d$ bands in $CeRhIn_5$ and $CeIrIn_5$.

References

1. Nakatsuji S, et al. (2002) Intersite coupling effects in a Kondo lattice. *Phys. Rev. Lett.* 89:106402.
2. Cornut B, Coqblin B (1972) Influence of the crystalline field on the Kondo effect of alloys and compounds with cerium impurities. *Phys. Rev. B* 5:4541.
3. Pruschke T, Bulla R, Jarrell M (2000) Low-energy scale of the periodic Anderson model. *Phys. Rev. B* 61:12799.
4. Burdin S, Georges A, Grempel DR (2000) Coherence scale of the Kondo lattice. *Phys. Rev. Lett.* 85:1048.
5. Vidhyadhiraja NS, Tahvildar-Zadeh AN, Jarrell M, Krishnamurthy HR (2000) "Exhaustion physics" in the periodic Anderson model from iterated perturbation theory. *Europhys. Lett.* 49:459.
6. Assaad FF (2004) Coherence scale of the two-dimensional Kondo lattice model. *Phys. Rev. B* 70:020402(R).
7. Burdin S, Zlatić V (2009) Multiple temperature scales of the periodic Anderson model: Slave boson approach. *Phys. Rev. B* 79:115139.
8. Yang Yf, Fisk, Z. L, Han-Oh, Thompson JD, Pines D (2008) Scaling the Kondo lattice. *Nature* 454:611.
9. Dudy L, et al. (2013) Yb valence change in $Ce_{1-x}Yb_xCoIn_5$ from spectroscopy and bulk properties. *Phys. Rev. B* 88:165118.
10. Nomoto T, Ikeda H (2014) Fermi surface evolution and d-wave superconductivity in $CeCoIn_5$: Analysis based on LDA + DMFT method. *Phys. Rev. B* 90:125147.
11. Reinert F, et al. (2001) Temperature dependence of the Kondo resonance and its satellites in $CeCu_2Si_2$. *Phys. Rev. Lett.* 87:106401.
12. Singley EJ, Basov DN, Bauer ED, Maple MB (2002) Optical conductivity of the heavy fermion superconductor $CeCoIn_5$. *Phys. Rev. B* 65:161101.
13. Lonzarich G, Pines D, Yang Yf (2017) Toward a new microscopic framework for Kondo lattice materials. *Rep. Prog. Phys.* 80:024501.
14. Aynajian P, et al. (2012) Visualizing heavy fermions emerging in a quantum critical Kondo lattice. *Nature* 486:201.
15. Gyenis A, et al. (2016) Quasiparticle interference of heavy fermions in resonant X-ray scattering. *Sci. Adv.* 2:e1601086.
16. Chen QY, et al. (2017) Direct observation of how the heavy-fermion state develops in $CeCoIn_5$. *Phys. Rev. B* 96:045107.
17. Willers T, et al. (2010) Crystal-field and Kondo-scale investigations of $CeMIn_5$ (M=Co, Ir, and Rh): A combined x-ray absorption and inelastic neutron scattering study. *Phys. Rev. B* 81:195114.
18. Chen QY, et al. (2018) Tracing crystal-field splittings in the rare-earth-based intermetallic $CeIrIn_5$. *Phys. Rev. B* 97:075149.
19. Allan MP, et al. (2013) Imaging Cooper pairing of heavy fermions in $CeCoIn_5$. *Nat. Phys.* 9:468.
20. Nakatsuji S, Pines D, Fisk Z (2004) Two fluid description of the Kondo lattice. *Phys. Rev. Lett.* 92:016401.
21. Yang Yf (2016) Two-fluid model for heavy electron physics. *Rep. Prog. Phys.* 79:074501.
22. Shim JH, Haule K, Kotliar G (2007) Modeling the localized-to-itinerant electronic transition in the heavy fermion system $CeIrIn_5$. *Science* 318:1615.
23. Yang Yf, Pines D (2008) Universal behavior in heavy-electron materials. *Phys. Rev. Lett.* 100:096404.
24. Koitzsch A, et al. (2013) Band-dependent emergence of heavy quasiparticles in $CeCoIn_5$. *Phys. Rev. B* 88:035124.
25. Settai R, et al. (2001) Quasi-two-dimensional Fermi surfaces and the de Haas-van Alphen oscillation in both the normal and superconducting mixed states of $CeCoIn_5$. *J. Phys.: Condens. Matter* 13:L627.
26. Shishido H, et al. (2002) Fermi surface, magnetic and superconducting properties of $LaRhIn_5$ and $CeTIn_5$ (T : Co, Rh and Ir). *J. Phys. Soc. Jpn.* 71:162.
27. Kirchner S, et al. (2020) Colloquium: Heavy-electron quantum criticality and single-particle spectroscopy. *Reviews of Modern Physics* 92:011002.
28. Shirer KR, et al. (2018) Dirac fermions in the heavy-fermion superconductors $Ce(Co,Rh,Ir)In_5$. arXiv:1808.00403.
29. Sun K, Yao H, Fradkin E, Kivelson SA (2009) Topological insulators and nematic phases from spontaneous symmetry breaking in 2d Fermi systems with a quadratic band crossing. *Phys. Rev. Lett.* 103:046811.
30. Burkov AA, Hook MD, Balents L (2011) Topological nodal semimetals. *Phys. Rev. B* 84:235126.